Trans Indian Inst Met (2020) 73(10):2435–2445
https://doi.org/10.1007/s12666-020-02045-0

ORIGINAL ARTICLE

Hot deformation behavior and optimization of processing parameters of a high-strength Mg-Gd-Nd-Zn-Sn-Zr alloy

Zehua Yan[1,2] · Yandong Yu[1,2] · Jiahao Qian[1,2] · Yanchao Sang[1,2] · Yiming Yao[1,2]

Received: 22 February 2020 / Accepted: 14 July 2020 / Published online: 31 July 2020

Abstract Aiming at the forward extrusion forming and its parameter optimization of high-strength and heat-resistant Mg-9Gd-3Nd-1Zn-1Sn-0.5Zr alloy, the isothermal compression stress–strain behavior was investigated. The high-temperature plastic deformation constitutive equation and the microstructure evolution of the alloy were obtained. According to the results of variation of stress–strain with strain rates and processing temperatures, a thermal processing map of the alloy was constructed, to obtain a safe processing area where the material is not prone to be unstable. Based on the results of thermal processing map, the experiments were carried out with the punching speed of 2 mm/s, the temperatures of 400 °C, 425 °C and 450 °C and the extrusion ratio of 12. The results showed that the best comprehensive properties of the alloy were obtained at the extrusion temperature of 425 °C. In addition, our findings were in good agreement with the prediction of the thermal processing map.

Keywords Mg-9Gd-3Nd-1Zn-1Sn-0.5Zr alloy · Microstructure · Constitutive equation · Thermal processing map · Extrusion

✉ Yandong Yu
yyd@hrbust.edu.cn

[1] Department of Materials Science and Engineering, Harbin University of Science and Technology, Harbin 150040, People's Republic of China

[2] Key Laboratory of Advanced Manufacturing and Intelligent Technology, Ministry of Education, Harbin 150040, People's Republic of China

1 Introduction

Casting is one of the remarkably important part in magnesium alloy forming method [1–3]. However, solidification defects and poor room temperature plasticity of as-cast magnesium alloys make them unsuitable to be applied in structural materials [4, 5]. High-temperature plastic deformation methods, such as extrusion, forging, rolling and other processes, are effective to prepare magnesium alloy products with improved mechanical properties and eliminating casting defects [6–13]. Meanwhile, elevated temperature can provide energy for activating the non-base surface slip and grain boundary slipping, and thus the plasticity of magnesium alloys is improved [14]. Relevant studies show that magnesium alloys are sensitive to strain rate and deformation temperature; therefore, deformation parameters are important to obtain more outstanding comprehensive performance of the products [15, 16].

Recently, various heat-resistant magnesium alloys have been successfully developed to meet the requirements of high strength, such as WE43 alloys, which have already been brought in to commercial use. With the development of Mg-RE alloys, lots of new alloys have been developed, especially for those with high Gd content [17–23]. However, addition of RE in magnesium alloy will increase costs. Considering that adding an appropriate amount of Sn to the Mg-RE alloys can promote the formation of high-temperature stable compounds, the strength of Mg-9Gd-3Nd-1Zn-1Sn-1Zr (wt%) alloy is improved with the addition of Sn to replace some RE in the present literature [24]. Furthermore, the isothermal compression test is an effective method to simulate the thermoplastic deformation characteristics of materials [25]. More importantly, those mathematical models can predict the quality of the processed products [26–30]. In this paper, based on the

thermal processing map, the predicted deformation temperature has been experimentally verified by using forward extrusion.

2 Materials and experiments

The Mg-9Gd-3Nd-1Zn-1Sn-0.5Zr (wt%) alloy was prepared in the 1% SF_6 and 99% CO_2 melting protective gas protection. It should be noted that the temperature of the whole smelting process was between 720 °C and 780 °C. As shown in Table 1, full-spectrum direct-reading inductively coupled plasma emission spectrometer (ICP) test result indicates that the test composition is close to the actual composition.

As shown in Fig. 1, the cylindrical samples (Φ15 mm × 10 mm) were cut for compression in a Gleeble-3500 thermal simulator from the homogenized alloy (treated at 525 °C for 10 h), and the heating temperatures were varied from 300 °C to 450 °C with an interval of 50 °C at a rate of 0.001 s^{-1} to 1 s^{-1}. When the sample was compressed to a true strain of 0.8, the test was stopped and it was cooled by water quenching. In addition, different temperatures were selected to verify the extrusion experiment. Microstructures of the alloy were characterized by OM (GX71), SEM (FEI SIRION 200), TEM (JEM-2000).

3 Results and discussion

3.1 Microstructure analysis of as-cast and solid-solution alloys

Figure 2a is the OM of as-cast Mg-9Gd-3Nd-1Zn-1Sn-0.5Zr alloy, and one can see that composition of the alloy mainly consists of equiaxed dendrites and eutectic compounds. The result shows that the grain size distribution is the relative bimodal with an average grain size of about 31 μm. In addition, many eutectic compounds are distributed in a continuous network along grain boundaries, and some granular second phases are found inside the matrix. Figure 2b shows the OM of the solid-solution alloy, and it shows that the amount of second phases in the solution treated alloy decreases obviously when compared with the as-cast alloy. But the eutectic compound at the

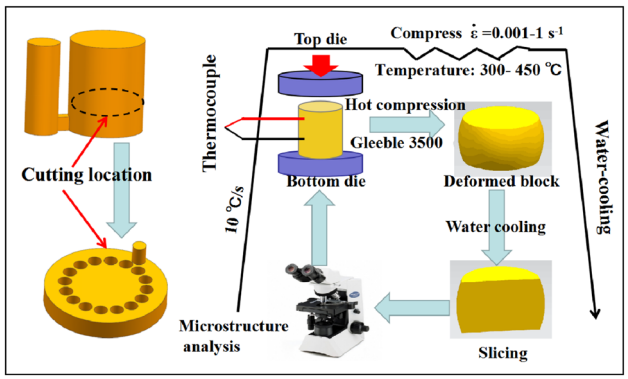

Fig. 1 Schematic diagram for selecting sample position and hot compression process

grain boundary gradually transforms into coarser phase, particularly at the trigeminal junction between grains. Figure 2c and Table 2 show the SEM image and EDS results of the as-cast alloy, where eutectic compounds are distributed in the grain boundary and grain interior, and the size of eutectic compounds varies greatly. These eutectic phases are composed of some sphere Mg_5(RE, Zn) phases with a diameter of about 5 μm, some square Mg_5(RE, Zn) phase with a side length of about 2 μm, and some Mg_2(Sn, Nd)$_3Gd_2$ particles. After solid-solution treatment, the segregation occurs at the grain boundary, and the Mg_5(RE, Zn) at the grain boundary is slightly connected into a continuous network. Besides, only few undissolved Mg_2(Sn, Nd)$_3Gd_2$ phases exist in its intragranular region (as shown in Fig. 2d and Table 2).

TEM was carried out to further determine the composition of the grain boundary precipitates in the solid-solution alloy, as shown in Fig. 3. According to the SAED pattern and Table 2, the grain boundary phase is close to the composition of Mg_5(RE,Zn) [31], but the content of RE is slightly higher than that of as-cast alloy.

4 Microstructure analysis of compressed alloy and its constitutive relation

Figure 4 shows the true stress–strain curves of Mg-9Gd-3Nd-1Zn-1Sn-0.5Zr alloy with unidirectional thermal compression. From these curves, one can see that the peak stress increases monotonously with decreasing

Table 1 Mass percentage of Mg-9Gd-3Nd-1Zn-1Sn-0.5Zr alloy measured by ICP

Elements	Gd	Nd	Sn	Zn	Zr	Mg
Nominal composition	9.00	3.00	1.00	1.00	0.50	Balanced
Actual composition	9.22	2.67	0.92	0.85	0.43	Balanced

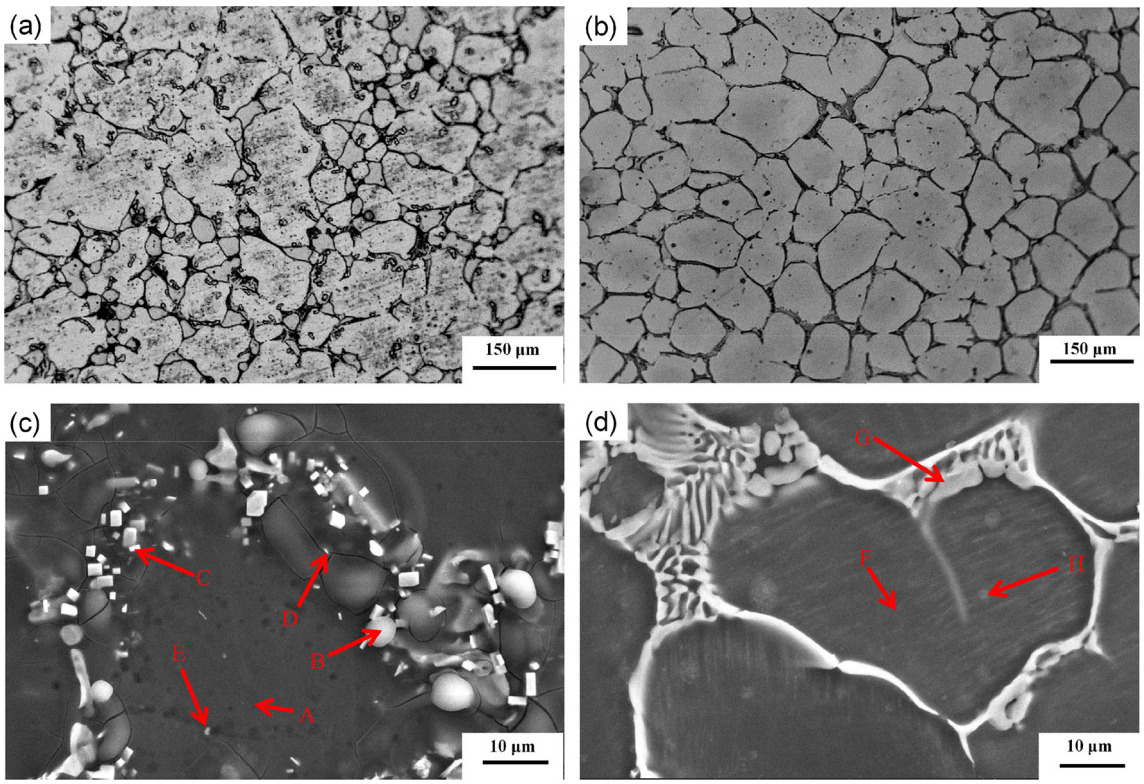

Fig. 2 OM and SEM image of Mg-9Gd-3Nd-1Zn-1Sn-0.5Zr alloy (**a**) and (**c**) as-cast, (**b**) and (**d**) solid-solution

Table 2 The EDS analysis of various types of the phases shown in Fig. 2(c) and (d)

Position	Composition (at.%)						Possible phases
	Mg	Gd	Nd	Zn	Sn	Zr	
A	96.89	2.14	0.28	0.21	0.25	0.23	α-Mg
B	79.86	9.12	4.21	6.41	0.32	0.08	Mg_5(RE, Zn)
C	82.05	8.28	5.07	4.25	0.09	0.26	Mg_5(RE, Zn)
D	33.43	29.87	14.73	0.15	21.67	0.15	$Mg_2(Sn, Nd)_3Gd_2$
E	28.61	31.27	16.52	0.19	23.22	0.19	$Mg_2(Sn, Nd)_3Gd_2$
F	95.35	2.05	2.17	0.18	0.13	0.12	α-Mg
G	77.05	12.66	5.67	4.25	0.21	0.16	Mg_5(RE, Zn)
H	66.23	15.65	8.16	0.27	9.47	0.22	α-Mg and $Mg_2(Sn, Nd)_3Gd_2$

temperature, indicating that work hardening is dominant at low temperatures. For a given temperature, the peak stress increases with the increasing strain rate, which indicates that the factors that weaken the work hardening such as dislocation accumulation will become more obvious at lower strain rates. Liu et al. revealed that the peak stress is an indication of the beginning to dynamic recrystallization (DRX) of alloys under corresponding deformation conditions [32]. For any curves, work hardening, dynamic recovery and dynamic recrystallization occur in turn, finally reaching dynamic equilibrium. At the beginning of hot compression, the stress value increases rapidly with the increase in deformation, which is related to an observable work hardening phenomenon. The reason is that, as the severity of the deformation increases, dislocation density and the formation of dislocation accumulation lead to the interaction of different dislocations in grains [33]. Meanwhile, the stress concentrates on grain boundaries, which increase the resistance to deformation and hinder the movement of dislocations. The effect of deformation softening is stronger than that of work hardening when the peak rheological value of the alloy reaches its maximum.

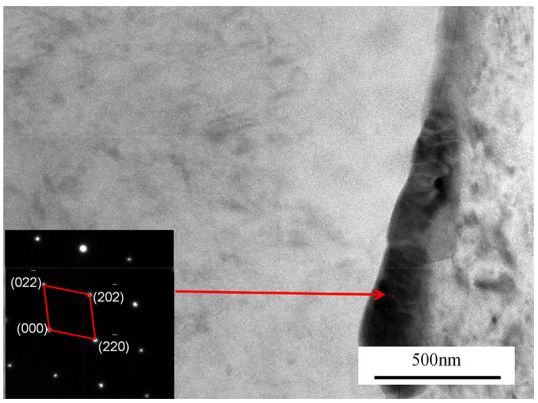

Fig. 3 Bright-field TEM image of grain boundary precipitates in the alloy after solid-solution and corresponding SAED pattern

At this point, the large angle grain boundary movement is due to dynamic recrystallization. This promotes numerous dislocations to annihilate, resulting in a slow decrease in flow stress of the alloy, and its growth rate continues to decline. Ultimately, the flow stress reaches a fixed value.

Strain rate is one of the sensitive factors on the plastic forming of materials. Adjusting strain rate will have obvious effect on material's microstructure [34]. The microstructure under hot compression at 400 °C is further analyzed via TEM, particularly for dislocations and recrystallized grains in compressed alloy, and results are shown in Fig. 5. As the deformation resistance is smaller at 0.001 s^{-1}, there is no dynamic recrystallization and the grains are still large. The grains are coarse, and there are dislocation pile-up groups in the grains (Fig. 5a), which are caused by the small strain rate and the low recovery. The increase in dislocation density and grain breakage caused by deformation is difficult to be eliminated by recovery. From Fig. 5b, one can find that microstructure evolution during deformation changes obviously at the strain rate of 0.01. Grains are elongated under this situation, and the number of dislocations in the grains is obviously reduced. However, precipitate dislocations are gathered at the grain boundary. As the strain rate increases to 0.1, dislocation entanglement gradually disappears and substructure becomes clear. Besides, sub-grain boundary is obvious to be detected, as shown in Fig. 5c. The profile of grain boundary becomes much clearer and more distinguishable when the strain rate is 1, and equiaxed small grains can be found, showing obvious recrystallization characteristics, as shown in Fig. 5d. This result shows that by keeping the temperature in a certain range, the microstructure of the alloy is mainly dynamic recovery at low strain rates, while the formation of dynamic recrystallization grains is promoted at high strain rate.

To study optimum deformation parameters of Mg-9Gd-3Nd-1Zn-1Sn-0.5Zr alloy, it is necessary to make clear its constitutive characteristics and establish relevant equations. Usually, the relationship between stress, strain and temperature is given by formulas (1), (2), and (3) [35].

$$\dot{\varepsilon} = A[\sinh(\alpha\sigma)]^n \exp\left(-\frac{Q}{RT}\right) \quad \text{for all } \sigma \tag{1}$$

$$\dot{\varepsilon} = A_1 \sigma^{n_1} \exp\left(-\frac{Q}{RT}\right) \alpha\sigma < 0.8 \tag{2}$$

$$\dot{\varepsilon} = A_2 \exp(\beta\sigma) \exp\left(-\frac{Q}{RT}\right) \alpha\sigma > 1.2 \tag{3}$$

Here A, A_1, A_2, n_1, n are the different material parameters, n is a stress index, and $\alpha = \beta/n_1$. Q represents the deformation activation energy (kJ/mol), T is temperature, K is

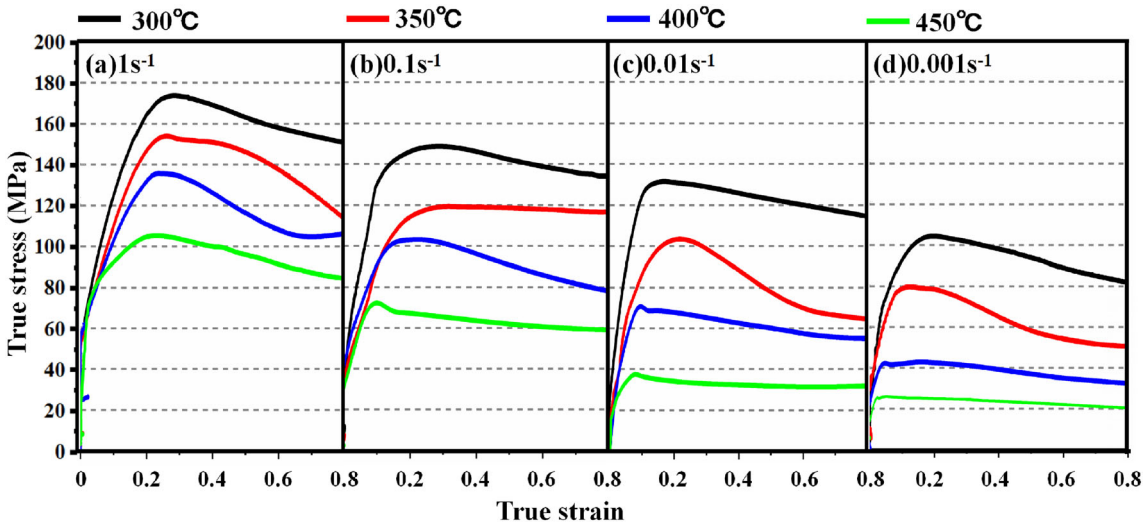

Fig. 4 True stress–strain curves of Mg-9Gd-3Nd-1Zn-1Sn-0.5Zr alloys under different deformation parameters (**a**) 1 s^{-1}, (**b**) 0.1 s^{-1}, (**c**) 0.01 s^{-1}, (**d**) 0.001 s^{-1}

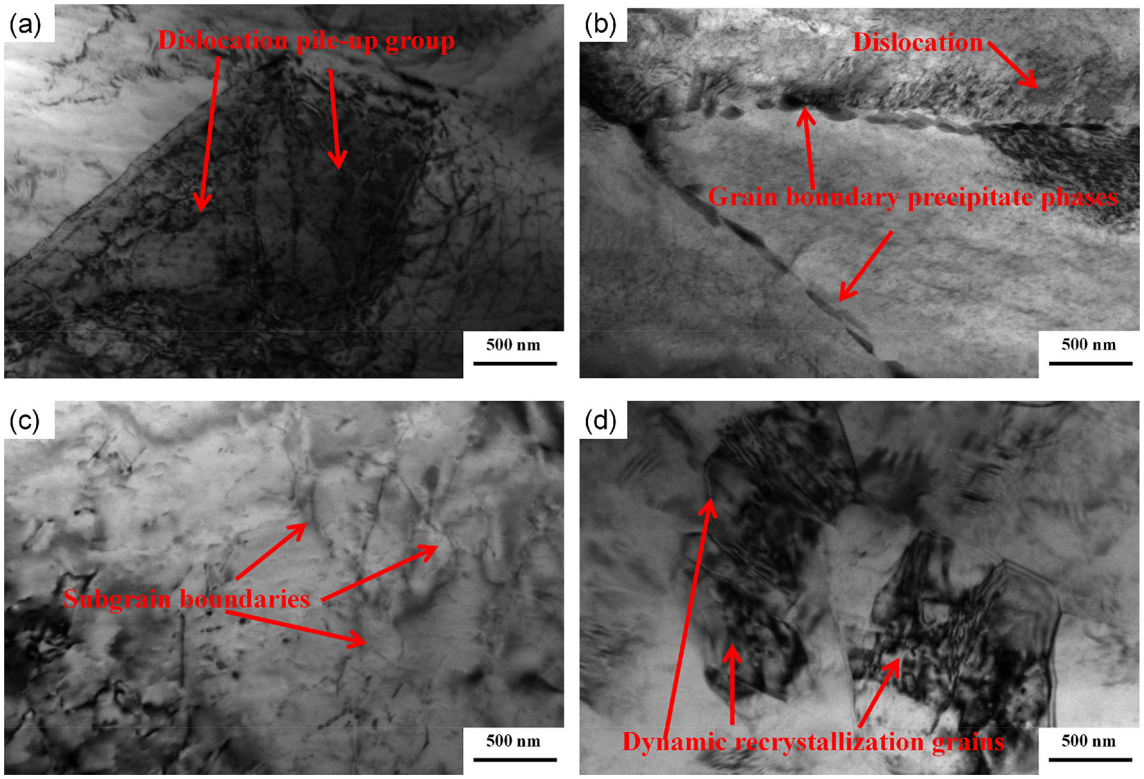

Fig. 5 TEM analysis for microstructure of hot compression alloy with different strain rates at 400 °C (**a**) 0.001 s^{-1}, (**b**) 0.01 s^{-1}, (**c**) 0.1 s^{-1}, and (**d**) 1 s^{-1}

rheological stress (MPa), and R is the ideal gas constant (8.314 J/mol).

By taking logarithms of formulas (1), (2) and (3) on both sides, the following relations are obtained. When the temperature is constant, the linear regression analysis of peak stress σ corresponding to the strain rate and $\ln\dot{\varepsilon}$ is carried out. According to above formulas, the slopes of fitting curves in Fig. 6a and b are values of β and n_1, respectively. The values of β and n_1 are calculated to be 0.087315 and 5.23865. Furthermore, α = 0.01667 MPa^{-1} is obtained.

As shown in Fig. 7, the value of N can be obtained by linear fitting diagrams of $\ln\dot{\varepsilon}$ and $\ln\sinh(\alpha\sigma)$, S can be obtained by the linear fitting diagrams of $\ln\sinh(\alpha\sigma)$ and $1/T$. The average slopes of all fitting curves in Fig. 7a and b are N = 5.9915 and S = 3.5017, respectively. According to Eq. (4), the deformation activation energy Q = 174.432 kJ/mol of Mg-9Gd-3Nd-1Zn-1Sn-0.5Zr alloy can be obtained.

$$Q = RNS \tag{4}$$

where $N = \left\{\frac{\partial \ln\dot{\varepsilon}}{\partial \ln[\sinh(\alpha\sigma)]}\right\}_T$ and $S = \left\{\frac{\partial \ln[\sinh(\alpha\sigma)]}{\partial(1/T)}\right\}_{\dot{\varepsilon}}$.

Under any stress, the influence of T and $\dot{\varepsilon}$ on the hot compression behavior of the alloy can be expressed by Zener and Hollomon relation, in which the parameter Z can be obtained from the hot working parameters [36].

$$Z = \dot{\varepsilon}\exp\left(\frac{Q}{RT}\right) \tag{5}$$

Combining Eqs. (4) and (5), we can get the following equation:

$$\ln Z = \ln A + n\ln[\sinh(\alpha\sigma)] \tag{6}$$

A linear fitting curve of $\ln Z$ and $\ln\sinh(\alpha\sigma)$ can be obtained by substituting the values of T, $\dot{\varepsilon}$ and σ_p, Q obtained above into Eq. (5), as shown in Fig. 8. The slope of the fitted curve is thus obtained from n and the intercept $\ln A$. Substituting the previously obtained values of Q, A, n, and α into Eq. (1), the constitutive equation of magnesium alloy under all stress conditions can be obtained. Obviously, this constitutive equation is applicable to a constitutive model with a deformation temperature of 300 °C to 450 °C and a strain rate of 0.001 s^{-1} to 1 s^{-1}. The constitutive equation of flow stress of Mg-9Gd-3Nd-1Zn-1Sn-0.5Zr alloy at high temperature is obtained as follows:

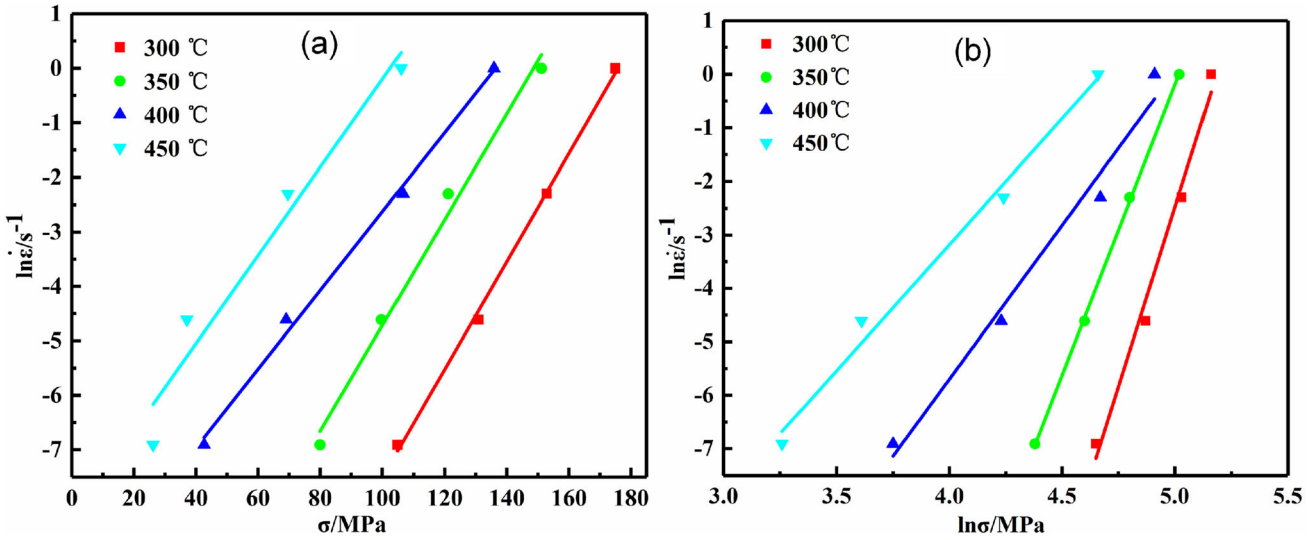

Fig. 6 Relationship between flow stress and strain rate during compression deformation for Mg-9Gd-3Nd-1Zn-1Sn-0.5Zr alloy. (**a**) σ and $\ln\dot{\varepsilon}$, (**b**) $\ln\sigma$ and $\ln\dot{\varepsilon}$

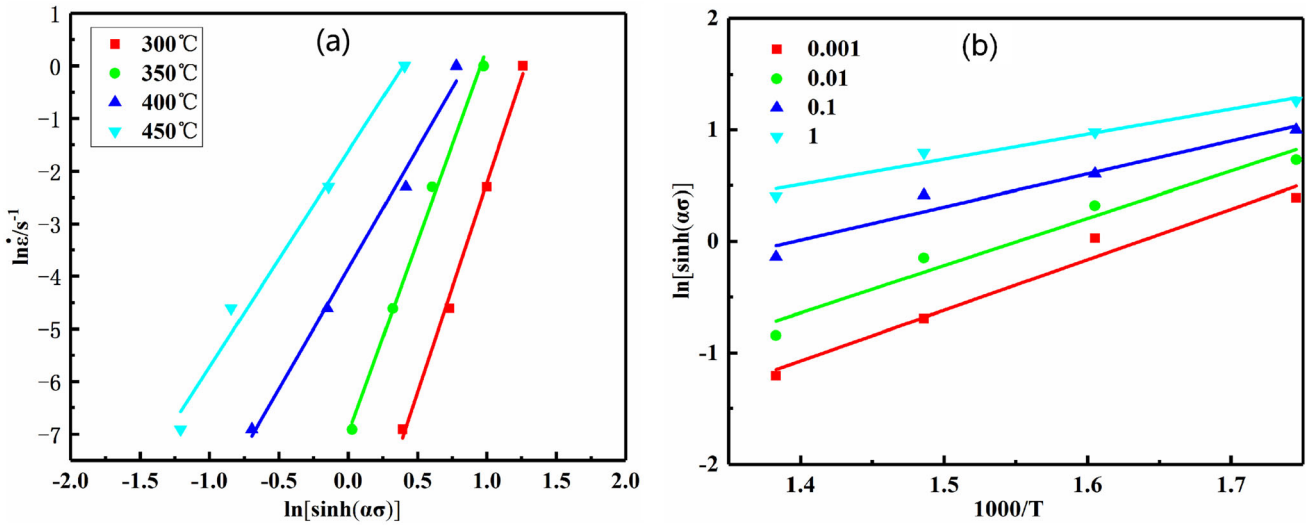

Fig. 7 Relationship of flow for Mg-9Gd-3Nd-1Zn-1Sn-0.5Zr alloy (**a**) stress and strain rate, (**b**) strain rate and temperature

$$\sigma_p = 123.12 \times \left\{ \left[\frac{Z}{1.226 \times 10^{12}} \right]^{\frac{1}{5.9915}} + \left[\left(\frac{Z}{1.226 \times 10^{12}} \right)^{\frac{2}{5.9915}} + 1 \right]^{\frac{1}{2}} \right\} \quad (7)$$

where the

$$Z = \dot{\varepsilon} \exp\left(\frac{174.432 \times 10^3}{RT} \right) \quad (8)$$

4.1 Thermal processing map analysis

According to the dynamic material model (DMM), the dissipation rate η for the tissue change energy during plastic deformation of the material can be described as Eq. 9 [34]:

$$\eta = \frac{2m}{m+1} \quad (9)$$

The rheological instability criterion for plastic deformation of materials is:

$$\xi(\dot{\varepsilon}) = \frac{\partial \ln\left(\frac{m}{m+1}\right)}{\partial \ln \dot{\varepsilon}} + m < 0 \quad (10)$$

Introducing three different temperature-dependent material parameters (a, b, c), the relationship between σ and $\ln\dot{\varepsilon}$ can be established to obtain the value of m, as shown in the following formula:

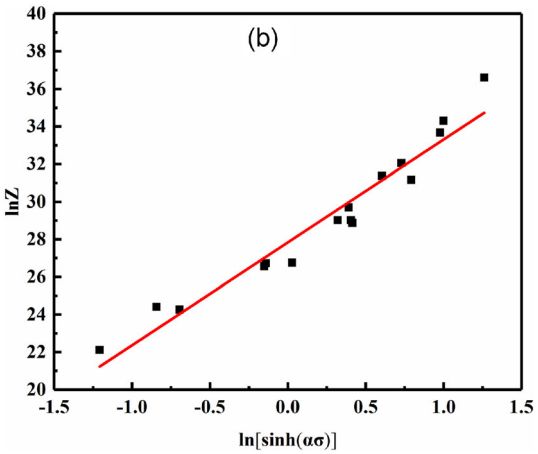

Fig. 8 Linear fittings of ln Z and $\ln\sinh(\alpha\sigma)$ at the strain of 0.8

$$m = \frac{\partial \ln \sigma}{\partial \ln \dot{\varepsilon}} = a + 2b\ln\dot{\varepsilon} + 3c\ln\dot{\varepsilon} \tag{11}$$

As mentioned above, σ and $\ln\dot{\varepsilon}$ satisfy the linear relationship, and it proves that the optimum deformation parameters of the Mg-9Gd-3Nd-1Zn-1Sn-0.5Zr alloy can be obtained by processing map. Figure 9a and b shows the 3D color mapping curved surfaces with projections of power efficiency and instability factors of the alloy under different process parameters on strains of 0.8. It can be concluded from Fig. 9a that three peaks are shown in the 3D power dissipation diagram, which is located near 350 °C with 1 s^{-1}, 395 °C with 0.001 s^{-1}, 450 °C with 0.01 s^{-1}, respectively. This means that more energy is dissipated when the alloy is plastically deformed in this region, which is beneficial to hot working. Figure 9b shows the 3D instability parameter diagram of the alloy, in which the instability parameter is made up of two parts, i.e. positive safety zone and negative instability zone. If the instability parameter is less than zero, it means that the properties are poor when the alloy is processed. Thus this area should be avoided as far as possible. Therefore, in order to obtain a better deformed alloy, the above two factors are taken into account comprehensively. Plastic deformation should be carried out in the region with larger dissipation value but no instability area. The thermal processing map shown in Fig. 9c can be obtained by superposition of energy dissipation diagram and instability diagram, and the numerical values on the contour line represent the energy consumption rate (η). Shadow area is the rheological instability area in the deformation process of experimental alloys. The area of $\dot{\varepsilon}<0$ drawn in the coordinate system is composed of $\ln\dot{\varepsilon}$ and T. The deformation in the instability area should be avoided as far as possible during the alloy forming. The contour value indicates the power consumption rate of the material, and the hatched area indicates the material deformation region where the instability is likely to occur. It can be seen that the strain has a great influence on the processing map with the strain value of 0.8. The safe area in the thermal processing map of the alloy can be divided into three areas based on the unstable areas namely: zones A, B and C. Zone A appears in the temperature from 340 °C to 370 °C with the strain rate ranging from 0.449 s^{-1} to 1 s^{-1} and the peak efficiency (about 0.39 s^{-1}) at 350 °C with 1 s^{-1}. Zone B appears in the temperature from 377 °C to 390 °C and the strain rate in a range of 0.001 s^{-1} to 0.042 s^{-1}. In addition, zone B also includes locations where the temperature is from 377 °C to 407 °C with the strain rate between 0.001 s^{-1} and 0.002 s^{-1}, but the peak efficiency (about 0.41) can be obtained at 390 °C with 0.003 s^{-1}. Zone C appears in the temperature from 435 °C to 450 °C with the strain rate in the range from 0.008 s^{-1} to 0.050 s^{-1}, and the peak efficiency is (about 0.41) at 440 °C with 0.030 s^{-1}.

To initially determine the optimal processing area, the microstructure of the compressed alloy with different parameters was analyzed, as shown in Fig. 10. At 350 °C with 1 s^{-1} (i.e. zone A), the microstructures are flattened and plastically deformed. No cracks or local rheological phenomena are found in the whole microstructure, the uniformity of grain size is poor, and only a few recrystallized grains are found, as shown in Fig. 10a and b. It confirms that the energy is mainly consumed in the deformation of the grain under this process. At 400 °C with 0.001 s^{-1} (i.e. zone B), small recrystallized crystal grains surround large crushed grains, as shown in Fig. 10c and d. Only a small amount of extremely fine recrystallized grains appear at the grain boundaries, especially in the trigeminal grain boundaries with severe deformation. This indicates that dynamic recrystallization has only occurred in a local area with a large degree of deformation. The reason for this phenomenon is that, the recrystallization process is a time-consuming process that requires not only sufficient deformation temperature to be driven, but also sufficient time to ensure that recrystallization proceeds. The low-temperature deformation cannot provide the driving force required for recrystallization nucleation. Owing to the severe deformation in the severely deformed area, the storage energy in this area will increase, and the nucleation of DRX grains will become more significant. At 450 °C with 0.01 s^{-1} (i.e. zone C), the corresponding microstructure is shown in Fig. 10e and f. Deformation rate of the alloy is slow, and the temperature is high enough; therefore, dynamic recovery and dynamic recrystallization are fully activated under this circumstance. The power dissipation rate of the alloy reaches 0.41. The amount of recrystallized grains at grain boundaries increases gradually, and the deformed structure is gradually replaced by new fine grains. Finally, a completely recrystallized structure is formed.

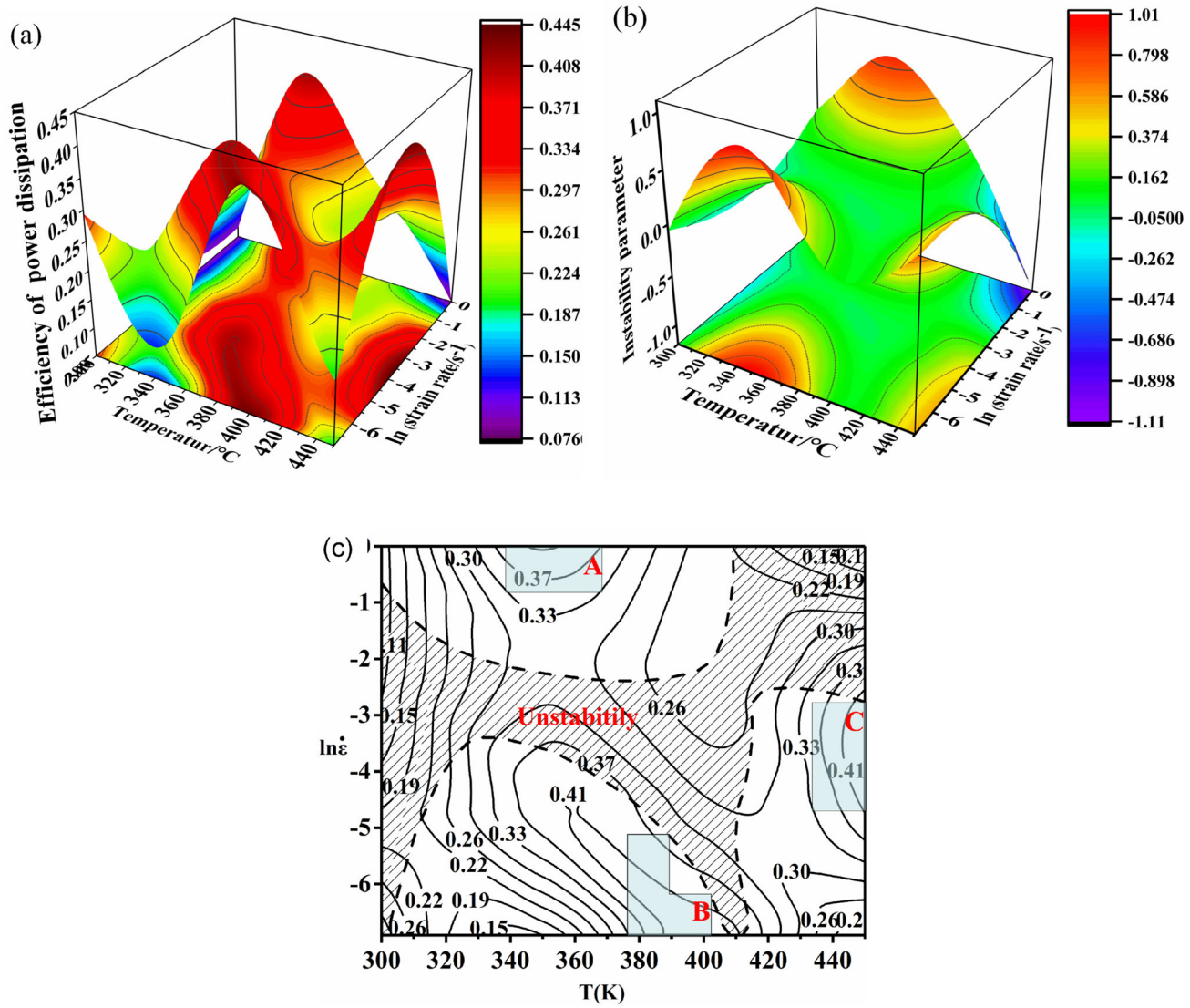

Fig. 9 Processing map of the Mg-9Gd-3Nd-1Zn-1Sn-0.5Zr alloy at true strain of 0.8 (**a**) power dissipation map. (**b**) instability map, and (**c**) the thermal processing map

4.2 Verification of magnesium alloy extrusion

According to the above analysis, the homogenized billets were placed in a mold with a lead angle and extruded to bars, as shown in Fig. 11a. To make the extrusion more smooth, three extrusion temperatures (400 °C, 425 °C, and 450 °C) were selected for extrusion tests. The starting point of the sizing belt as the origin of the coordinate axis, the X axis as the extrusion direction, and the Y axis as the radial direction were picked up. Then the diameter at the distance x from the origin in the cone deformation area is y. In the reducing area of extrusion, α is the semi-angle, and d_0 is the diameter when semi-angle begins to change; the following formula (12) can be calculated from the geometric conditions:

$$y = d_0 - 2x \times \tan\alpha \tag{12}$$

Setting the extrusion speed to v, then Eq. (13) is as following:

$$v = \frac{\mathrm{d}x}{\mathrm{d}t} \tag{13}$$

According to the definition of volume invariance before and after extrusion, Eq. (14) can be calculated:

$$\varepsilon = \frac{L - L_0}{L} = 1 - \frac{L_0}{L} = 1 - \frac{S}{S_0} = 1 - \frac{D^2}{y^2} \tag{14}$$

where L_0 and L are the length of the billet before extrusion and the finished product after extrusion, respectively, D and y are the cross-sectional diameter before and after extrusion, respectively. Extrusion is a type of non-uniform

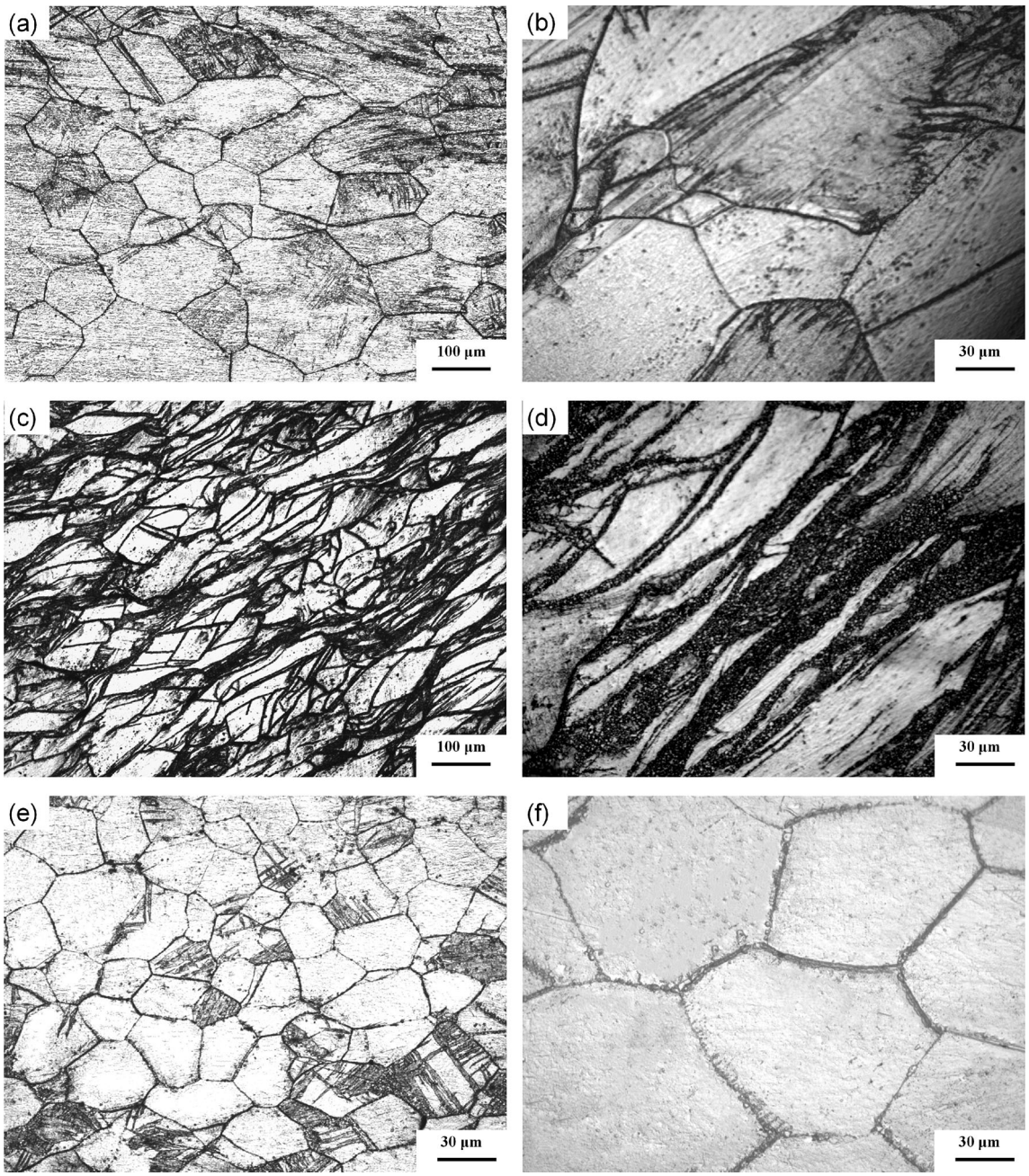

Fig. 10 Typical microstructures of the deformed specimens located at the corresponding domains of the processing maps. (**a**, **b**) at 350 °C with 1 s^{-1} in zone A, (**c**, **d**) at 400 °C with 0.001 s^{-1} in zone B, and (**e**, **f**) at 450 °C with 0.01 s^{-1} in zone C

deformation mode, so the strain is different on both billet and extrusion bar. Using the extrusion speed as a factor, the average strain rate of the alloy during extrusion can be calculated by the following formula:

$$\dot{\varepsilon} = \frac{\mathrm{d}\varepsilon}{\mathrm{d}t} = -\frac{2y\mathrm{d}y}{D^2\mathrm{d}t} = \frac{2y(-2\tan\alpha)\mathrm{d}x}{D^2\mathrm{d}t} = \frac{4v(\tan\alpha)\times(d_0 - 2x\tan\alpha)}{D^2} \quad (15)$$

When the alloy is extruded from the mold, the value of x is 9. So combining the optimal strain rates (from 0.008 s^{-1} to 0.05 s^{-1}) and the extrusion parameters of the alloy (as shown in Table 3), it can be estimated form formula (15) that the optimal value of v is between 0.32 mm/s and 2.00 mm/s. In this experiment, the punching speed was selected as 2 mm/s.

Schematic diagram of the extrusion die and extruded bars is presented in Fig. 11. When the alloy is extruded at 400 °C, there is a large tear crack at the surface of the bars, and the fracture does not show obvious oxidation.

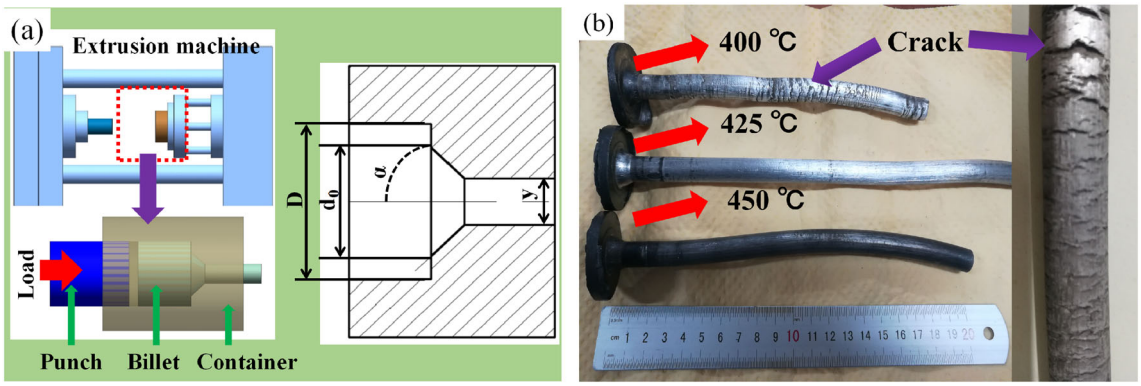

Fig. 11 (**a**) Model of the extrusion die, and (**b**) extruded bars at the extrusion temperature of 400 °C, 425 °C, 450 °C, respectively

Table 3 Extrusion data for Mg-9Gd-3Nd-1Zn-1Sn-0.5Zr alloy

Code-named	*D*	*d*	α	d_0
Value (unit)	42 mm	12 mm	π/4	28 mm

Although the bar is successfully extruded at the lower temperature, the billet has a large difference in flow velocity between the core and the edge. It leads to the tear of the billet under the large pressure and the formation of cracks. When extruded at 450 °C, no holes, cracks and other defects are found on the surface of the products, while the oxidation is obvious on the surface. This is mainly due to high extrusion temperature, which causes significant temperature rise during the extrusion process. In such case, the extruded alloy is easily oxidized in the air. When extruded at 425 °C, the surface of the products is smooth during filling and extrusion. This also indicates that the thermal deformation parameter of the Mg-9Gd-3Nd-1Zn-1Sn-0.5Zr alloy extruded at 425 °C is reasonable.

5 Conclusions

By analyzing isothermal compression experiments, we studied the thermal compression stress and the microstructure evolution of homogenized Mg-9Gd-3Nd-1Zn-1Sn-0.5Zr alloy. Besides, the extrusion parameters of the experimental magnesium alloy are optimized by hot compression experiment. The conclusions are as follows:

1. Maintaining the temperature in a certain range, the crystal of the alloy is mainly dynamic recovery at low strain rates, while the formation of dynamic recrystallization grains is promoted at high strain rate. No matter what strain rate, the peak stress increases with the decrease in the temperature, indicating that work hardening is dominant at lower temperature. When the deformation temperature is fixed, the peak stress increases with the increase in the strain rate, which indicates that dislocation accumulation and weakening of the work hardening are more obvious at the relatively low strain rate.
2. The constitutive equation for hot compression deformation of homogenized alloys is as follows: $\sigma_p = 123.12 \times \left\{ \left[\frac{Z}{1.226\times10^{12}} \right]^{\frac{1}{5.9915}} + \left[\left(\frac{Z}{1.226\times10^{12}} \right)^{\frac{2}{5.9915}} + 1 \right]^{\frac{1}{2}} \right\}$, and the deformation activation energy is calculated to be 174.456 kJ/mol.
3. The thermal processing diagram shows that the smaller the strain rate, the higher the power consumption value of the alloy, and the maximum power consumption rate occurs at the range of deformation temperature from 420 °C to 450 °C and strain rates between 0.008 s^{-1} and 0.05 s^{-1}. Hot extrusion experiment indicates that extruding at 425 °C and 2 mm/s is reasonable.

Acknowledgments This work is supported by the Research and development project of scientific and technological achievements in provincial universities of Heilongjiang provincial department of education (Grant Number TSTAU-R2018003), open research fund of state key laboratory of metastable materials science and technology of Yanshan University (Grant Number 202002).

References

1. Men H, Jiang B, and Fan Z, *Acta Mater* **58** (2010) 6526.
2. Du Y-Z, Qiao X-G, and Zheng M-Y, *Mater Des* **85** (2015) 549.
3. Jiang W-M, Fan Z-T, and Liao D-F, *Int J Adv Manuf Technol* **51** (2010) 25.
4. Patel J-B, Yang X, and Mendis C-L, *JOM* **69** (2017) 1071.
5. Song B, Huang G-S, a Li H-C, *J Alloys Compd* **325** (2013) 325.
6. Park S-H, Kim H-S, Bae J-H, *Scripta Mater* **69** (2013) 250.
7. Wang H-Y, Yu Z-P, and Zhang L, *Sci Rep-UK* **5** (2015) 17100.
8. Panigrahi S-K, Yuan W, and Mishra R-S, *Sci Eng A-Struct* **530** (2011) 28.

9. Zhou X-J, Liu C-M, and Gao Y-H, *Mater Charact* **135** (2018) 76.
10. Zhi C-C, Ma L-F, and Huang Q-X, *J Mater Process Technol* **255** (2018) 333.
11. Rong W, Zhang Y, and Wu Y-J, *Mater Charact* **131** (2017) 380.
12. Tork N-B, Razavi S-H, and Saghafian H, *J Mater Sci Technol* **33** (2017) 2244.
13. He J-H, Jin L, and Wang F-H. J *Magnes Alloys* **5** (2017) 423.
14. Smith L, and Farkas D, *Comp Mater Sci* **147** (2018) 18.
15. Choi I, Lee D, and Ahn B, *Scripta Mater* **94** (2015) 44.
16. Mu Y-L, Wang Q-D, and Hu M-L, *Scripta Mater* 68 (2013) 885.
17. Sha X-C, Xiao L-R, and Chen X-F, *Philos Mag* **99** (2019) 1957.
18. Wang C-L, Wu G-H, and Lavernia E-J *J Mater Sci*, **52** (2017) 1831.
19. Cheng P, Zhao Y-H, and Lu R-P, *Mat Sci Eng A-Struct* **708** (2017) 482.
20. Casari D, Mirihanage W-U, and Falch K-V, *Acta Mater* **116** (2016) 177.
21. Liu N-Y, Zhang Z-Y, and Peng L-M, *Mat Sci Eng A-Struct* **627** (2015) 223.
22. Lyu S-Y, Xiao W-L, and Zheng R-X, *Mat Sci Eng A-Struct* **732** (2018) 178.
23. Li D-Q, Wang Q-D, and Ding W-J, *J Mater Sci* **44** (2009) 3049.
24. Kim Y-H, Kim J-H, and Yoo H-S. *J Nanosci Nanotechnol* **16** (2016) 11277.
25. Zhou H, Ye B, and Wang Q-D, *Mater Lett* **83** (2012) 175.
26. Hayes B-J, Martin B-W, and Welk B, *Acta Mater* **133** (2017) 120.
27. Li H-Y, Hu J-D, and Wei D-D, *Mater Design* **42** (2012) 192.
28. Wang F-Z, Zhao J, and Zhu N-B, *J Mater Eng Perform* **25** (2016) 4875.
29. Lin X-B, Zhai F-B, and Feng J-H. *J Mater Process Technol* **122** (2002) 38.
30. Xue Y, Zhang Z-M, and Lu G. *J Mater Eng Perform* **24** (2014) 964.
31. Liu Y, Kang Z-X, and Zhang J-Y, *Adv Eng Mater* **18** (2016) 833.
32. Liu G, Xie W, and Wei G-B, *Materials* **11** (2018) 408.
33. Wang Y-B, Ho J-C, and Cao Y, *Appl Phys Lett* **94** (2009) 091911.
34. Lv B-J, Peng J, and Wang Y-J, *Mater Design* **53** (2014) 357.
35. Kai X-Z, Zhao Y-T, and Wang A-D, *Compos Sci Technol* **116** (2015) 1.
36. Zhou Z-H, Fan Q-C, and Xia Z H, *J Mater Sci Technol*, **33** (2017) 637.